Flutter Prediction Report in Support of the High Angle Working Group at the Third Aeroelastic Prediction Workshop

Pawel Chwalowski,* Bret K. Stanford,† and Kevin E. Jacobson*
NASA Langley Research Center, Hampton, VA, 23681

Lior Poplingher‡ and Daniella E. Raveh§
Technion-Israel Institute of Technology, Haifa, 3200003, Israel

Adam Jirasek¶ and Jurgen Seidel‖
High Performance Computing Research Center, USAFA

Giampaolo Pagliuca**, Jose N. Berberoff-Naval††, and Matt Forster**
BAE Systems Air, Bristol, BS34 7QW, United Kingdom

Marcello Righi‡‡, Gabriele Immordino§§, and Andrea Da Ronch¶¶
Zurich University of Applied Sciences and *University of Southampton*

Steven E. Lamberson*** and Daniel Prosser†††
Bowhead Total Enterprise Solutions LLC, Springfield, VA 22150 and *NAWCAD Patuxent River, MD 20670*

Ettore Fadiga, Stefano Oliani, Francesco Rondina‡‡‡, and Luigi Capone§§§
Leonardo Labs, Leonardo S.p.A., Via Pieragostini, 80, Genova, Italy

This paper presents a summary of the computational flutter results associated with the AIAA third Aeroelastic Prediction Workshop (AePW-3) High Angle Working Group (HAWG). The computational results are compared against the experimental data collected during the Pitch and Plunge Apparatus (PAPA) Benchmark Supercritical Wing (BSCW) test campaign conducted in the Transonic Dynamics Tunnel (TDT) at NASA Langley Research Center thirty years ago. During that test several flutter points were identified at transonic conditions. One of these points, specifically near Mach 0.8 and 5° angle of attack, became a focal point of the computational challenge within HAWG. Various fidelity time-domain, Reduced Order Model (ROM) and Linearized Frequency Domain (LFD) methods were used by seven participating teams. While there are encouraging trends in the computational results, the range of the predicted flutter dynamic pressure is still quite large due to the stall flutter mechanism. A description of each participating team's software and methods is included.

*Research Engineer
†Research Engineer, AIAA Associate Fellow.
*Research Engineer, AIAA Member.
‡Graduate Student, Faculty of Aerospace Engineering.
§Professor, Faculty of Aerospace Engineering, AIAA Associate Fellow.
¶Senior Research Engineer, AIAA Member.
‖Research Director, AIAA Member.
**Research Scientist - Computational Engineering.
††Graduate Student - Computational Engineering.
**Research Scientist - Computational Engineering.
‡‡Professor, Lecturer at Federal Institute of Technology Zurich ETHZ1, AIAA Member.
§§PhD Student
¶¶Associate Professor, AIAA Senior Member.
***HITS-R2 / CREATE-AV Kestrel Principal Developer; AIAA Senior Member.
†††Aerospace Engineer, Applied Aerodynamics Branch, Patuxent River, MD, AIAA Member
‡‡‡Research Fellow.
§§§Head of Digital Twin and Advanced Simulation Lab

I. Introduction

The first two Aeroelastic Prediction Workshops (AePWs), held in 2012 [1] and 2016 [2], respectively, served as focal points for the aeroelastic community to compare their computational aeroelasticity tools and predictive capabilities. During the 2019 International Forum on Aeroelasticity and Structural Dynamics (IFASD2019) conference, the community decided to organize a third workshop (AePW-3), to be held at the AIAA SciTech 2023 conference. However, the subsequent meetings showed different interests among the aeroelastic community, so workshop activities [3] were split into four working groups: the Large Deflection Working Group (LDWG), the Flight Test Working Group (FTWG), the High Speed Working Group (HSWG), and the High Angle Working Group (HAWG). The LDWG focuses on analysis of the coupled aeroelastic problems associated with large deflections of a relatively flexible and high aspect ratio wing subjected to low-speed aerodynamics. The FTWG focuses on the body freedom flutter analysis of the NASA experimental flight vehicle X-56A. The HSWG focuses on fluid-structure-interaction analysis at high supersonic to hypersonic speeds, and the HAWG concentrates on the transonic flutter and shock-buffet computations on the Benchmark Supercritical Wing (BSCW) configuration at high angles of attack.

The cases selected for the HAWG are listed in Table 1. In this paper, the analysis results for Case #1 are presented. The results for Case #2 are presented in a separate paper [4]. Note that OTT, under the Case #2 heading, stands for the Oscillating Turntable and will be described later. The selection of the flutter case was motivated by several factors. First, the results from the second Aeroelastic Prediction Workshop, Case #3c at Mach 0.85 and angle of attack 5°, showed the difficulty in predicting flutter onset in the presence of the separated flow at the transonic condition [2]. Second, a cluster of three experimental data points is available near a condition chosen for flutter-prediction challenge [5]. This experimental point is at the flow condition deemed to be 'easier' to analyze than the flow conditions for a blind challenge from the second Aeroelastic Prediction Workshop. Third, there is a need for additional flutter experimental data across Mach number and angle-of-attack range. An anticipated retest of the BSCW wing in the Transonic Dynamics Tunnel (TDT) that will include modern optical methods, is scheduled for Spring 2025. Lastly, there is an implied connection between shock-buffet onset and a flutter event at condition selected for the AePW-3 [6], [5].

The seven teams contributing to the flutter predictions are: NASA Langley–Aeroelasticity Branch, Technion–Israel Institute of Technology, United States Air Force Academy (USAFA), BAE Systems Air, Zurich University of Applied Sciences and Southampton University, CREATE-AV and Naval Air Warfare Center Aircraft Division (NAWCAD), and Leonardo Labs. Some of these teams have already published their own papers on their computational flutter predictions [7], [8], [9], [10], [11]; therefore, this report concentrates on presenting comparison results only.

This paper is organized in three sections. Background material on the BSCW configuration and experimental setup with flow conditions are presented first. The process used in the analysis of the numerical results, followed by flutter dynamic pressure and flutter frequency results from each participating team together with the interpretations of these results are presented next. The last section contains a description of each team's numerical processes to compute flutter.

Table 1 AePW-3 HAWG Workshop Test Cases.

	Case #1	Case #2
Mach	0.8	0.8
AoA	5°	5°
Dynamic Data Type	Flutter Unsteady	Unforced Unsteady
Notes	- Attached / Separated - PAPA exp. data - R-134a	- Shock buffet (?) - OTT exp. data - R-134a

II. BSCW Wing Configuration

The BSCW model, shown in Figure 1, has a simple, rectangular, 16- x 32-inch wing planform, with a NASA SC(2)-0414 airfoil. It was first tested in the TDT in 1991 [12]. For this test, the wing was mounted on the TDT Pitch and Plunge Apparatus (PAPA) to obtain the flutter boundary at various Mach numbers and angles of attack for this two-degree of freedom (pitch and plunge) system. In 2000, the wing was tested again, this time on an OTT [13]. The purpose of the OTT tests was to measure aerodynamic response during sinusoidal (forced) pitch oscillation of the wing.

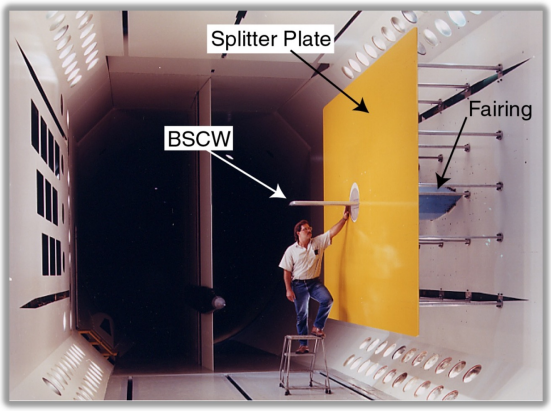

(a) BSCW model mounted on the OTT in TDT [1].

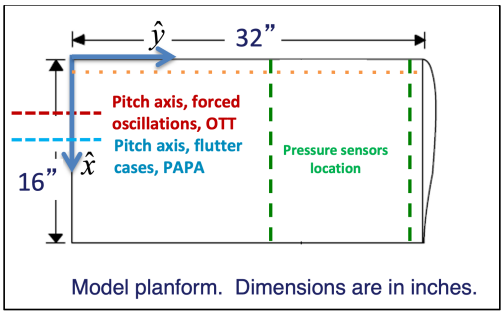

(b) BSCW geometry details.

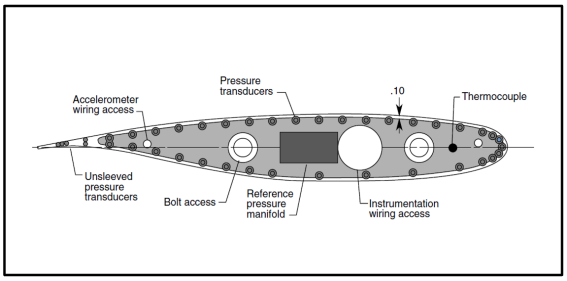

(c) BSCW instrumentation: SC(2)-0414 airfoil.

Chord	c_{ref}	16 in
Span	b	32 in
Area	A	512 in^2
Moment reference	x	4.8 in
	y	0 in
	z	0 in

(d) BSCW reference quantities.

Fig. 1 BSCW Model.

The experimental data indicated that the BSCW exhibited a strong shock and separated flow at moderate angles of attack at transonic conditions. The computations of the transonic flow, in conjunction with the flutter boundary predictions, were the focus of the second workshop [2]. The OTT test also provided some experimental data for the computational analysis of the shock-buffet environment. Specifically, before each forced oscillation test the wing was set at a fixed angle of attack and the unsteady pressure data was collected.

For both the OTT and PAPA tests, the model was mounted to a strut and sufficiently offset from the wind-tunnel wall (40 inches) via a large splitter plate, to (1) place the wing closer to the tunnel centerline and (2) be outside the tunnel wall boundary layer [14]. The wing was designed to be rigid, with the following structural frequencies for the combined wing and OTT mounting system: 24.1 Hz (spanwise first bending mode), 27.0 Hz (in-plane first bending mode), and 79.9 Hz (first torsion mode). When installed on the PAPA mount, the combined system frequencies were 3.33 Hz for the plunge mode and 5.20 Hz for the pitch mode [15]. The plunge and pitch modes are the only modes considered in the aeroelastic analyses of the PAPA-mounted configuration.

For instrumentation, the model has pressure ports in chordwise rows at the 60% and 95% span locations. For the BSCW/PAPA test, both rows were fully populated with unsteady in situ pressure transducers. The quantitative information obtained consists of unsteady data at flutter points and averaged data on a rigidized apparatus at the flutter conditions. For the BSCW/OTT test, only the inboard row at 60% span was populated with transducers. The quantitative information for the OTT test consists of unsteady pressure data and accelerometer data for forced pitch oscillations and for the static system at constant flow conditions. The analysis of the OTT experimental data is described in Reference [6].

Detailed flow conditions across the range of dynamic pressures were generated using the TDT tunnel parameter code and are shown in Table 2. It is important to note that NASA has plans to retest BSCW on the PAPA in the TDT in year 2025 and to utilize modern optical experimental methods, with the hope of providing additional experimental data for computational aeroelasticity software validation.

Table 2 BSCW flow conditions: Mach 0.8 with range of dynamic pressure (q); chord Reynolds number (Re_c); Reynolds number per foot (Re); velocity (V); speed of sound (a); static temperature, (T_{static}); density (ρ); ratio of specific heat (γ); viscosity (μ); Prandtl number (Pr); total pressure (H); and static pressure (P).

Mach	0.799	0.8	0.8	0.8	0.8	0.8	0.8	0.8	0.8	0.8	0.8	0.801	0.801
q [psf]	10.02	25.00	35.00	50.00	75.00	100.00	134.00	143.00	152.00	168.80	200.00	225.00	250.00
Re_C	237461	592224	829213	1184801	1777732	2371336	3178880	3392751	3606668	4006103	4748658	5343835	5939368
Re [1/ft]	178096	444168	621910	888601	1333299	1778502	2384160	2544563	2705001	3004577	3561493	4007876	4454526
V [ft/s]	440.45	440.63	440.59	440.51	440.39	440.21	440.05	440.00	439.96	439.88	439.70	439.58	439.46
a [ft/s]	551.08	550.94	550.85	550.71	550.48	550.25	549.94	549.86	549.78	549.62	549.34	549.11	548.88
T_{static} [$^\circ F$]	80.87	80.83	80.83	80.82	80.81	80.80	80.78	80.77	80.77	80.76	80.74	80.73	80.71
ρ [slug/ft^3]	0.000103	0.000258	0.000361	0.000515	0.000774	0.001032	0.001384	0.001477	0.001571	0.001745	0.002069	0.002329	0.002589
γ	1.1121	1.1122	1.1123	1.1124	1.1126	1.1128	1.1131	1.1131	1.1132	1.1133	1.1136	1.1138	1.1139
μ [lb-sec/ft^2]	2.555e-07	2.555e-07	2.555e-07	2.555e-07	2.555e-07	2.555e-07	2.554e-07	2.554e-07	2.554e-07	2.554e-07	2.554e-07	2.554e-07	2.554e-07
Pr	0.68394	0.68404	0.68410	0.68419	0.68435	0.68450	0.68471	0.68477	0.68483	0.68493	0.68513	0.68528	0.68544
H [psf]	40.00	99.72	139.61	199.45	299.18	399.00	534.69	570.61	606.53	673.59	798.21	898.01	997.83
P [psf]	28.21	70.32	98.45	140.64	210.97	281.37	377.05	402.38	427.71	475.00	562.87	633.25	703.64

III. Results and Conclusions

Each participating team was asked to provide computed time histories of the wing response: plunge (also called heave) and pitch modes at several dynamic pressure values, q. The method used to analyze that data is described next. Note, that in addition to time-domain methods, two teams computed flutter q using frequency-domain methods and one team employed reduced order modeling. The frequency-domain results are presented only in the sections describing individual team methods.

The matrix pencil method [16, 17] is used to analyze the time-domain and Reduced Order Models (ROM) aeroelastic response data. The method decomposes evenly spaced samples of the signal, $z_n = z(n\Delta t)$, into a Prony series plus a noise term:

$$z_n = \sum_{k=0}^{M-1} c_k e^{s_k n} + w_n, \qquad n = 0, 1, \ldots, N-1 \tag{1}$$

where the complex coefficient, c_k, represents an amplitude ($a_k = \mathrm{mod}(c_k)$) and phase ($\phi_k = \arg(c_k)$); the complex exponent, $s_k = (\alpha_K + i\omega_k)\Delta t$, contains the growth rate and frequency; w_n is the noise term; and M is the model number. The model number is the number of terms in the truncation of an infinite Prony series and filters the noise from the primary signal components of interest. The number of retained samples is selected via filtering of the Hankel matrix singular values, as described in [16]. In this analysis, the number of singular values kept is manually selected for each signal based on plots of singular values on a logarithmic scale.

As illustrated in Figure 2a, there is typically an observable difference between the relatively large jumps between the true components of the signal and the gradual decay of the noise components. Once the signal is decomposed by the matrix pencil method, the resulting Prony series is then used to compare a reconstruction of the signal to the original signal as illustrated in Figure 2b. The reconstruction is not exact because there is some nonlinearity at this complex condition; however, if reconstruction matches reasonably well with the original signal, the damping ratio and frequency are then determined from s_k for each component of the Prony series representation.

The matrix pencil process is applied to the second mode (the pitch mode) for all of the participants' results. Figure 3 and Figure 4 show the frequency and damping of the responses. Many of the pitch mode responses can be approximately reconstructed with 3 Prony series components: a zero frequency offset, and a pair of terms representing the positive and negative frequency parts of a single damped sinusoid. For signals that required multiple sinusoidal terms to reconstruct, the primary component was selected as the term with the minimum (most unstable) damping; this component corresponded to the term closest to wind-off pitch frequency in all cases. The responses are near the wind-off pitch frequency with slightly decreasing frequency as dynamic pressure increases. The flutter point is soft and very sensitive due to the damping curves generally being very shallow. Many of the results are within ±0.5% damping over a dynamic pressure range of 125 psf.

Since the participants applied various forms and amplitudes of perturbation, and the FUN3D RANS results (see subsection IV.A below) in Figure 4 show a dependence on amplitude of generalized velocity perturbation, the amplitude of the response is considered in the data processing. The amplitude is measured as the range (difference of the maximum and minimum) of the pitch angle over the first cycle of motion in the analysis window. The comparisons do not uncover a consistent trend across the participants' results when considering amplitude and are not presented here.

A cursory analysis focusing on the predicted flutter points, which range from $q = 0$ to 250 psf, would indicate that

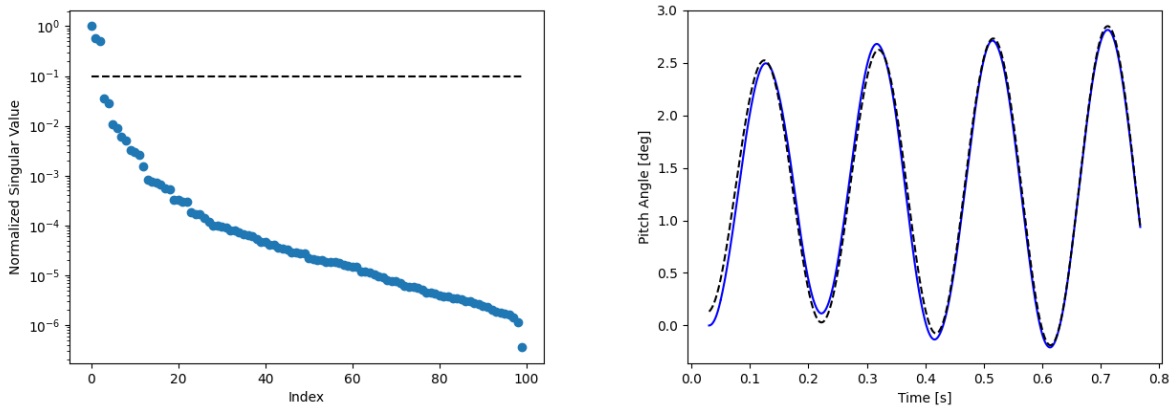

(a) Singular values normalized by the largest value.

(b) Final curve fit.

Fig. 2 Sample results from matrix pencil process applied to the flutter data.

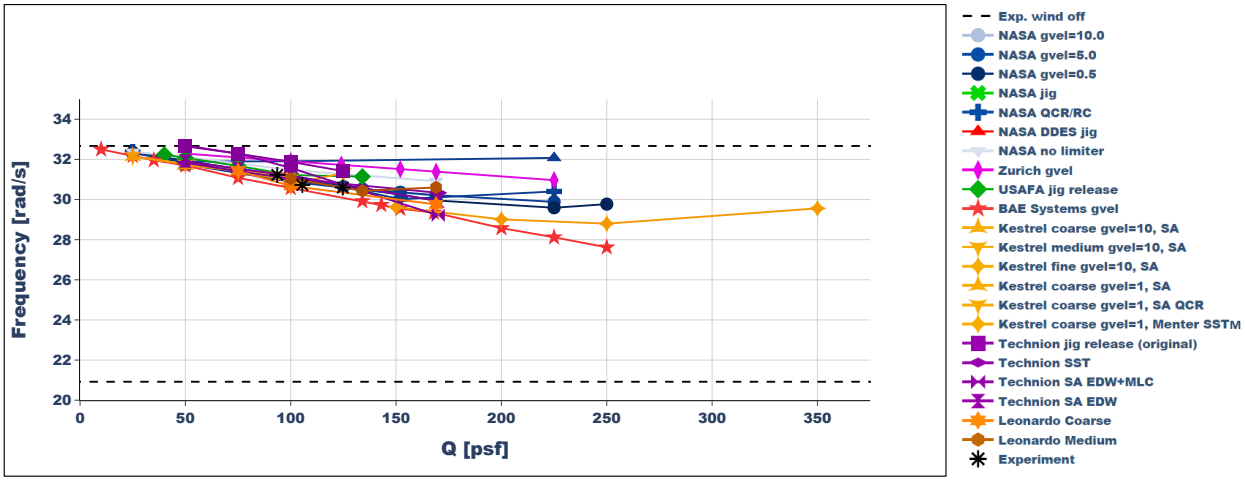

Fig. 3 Frequency of the primary component of the pitch response: all teams.

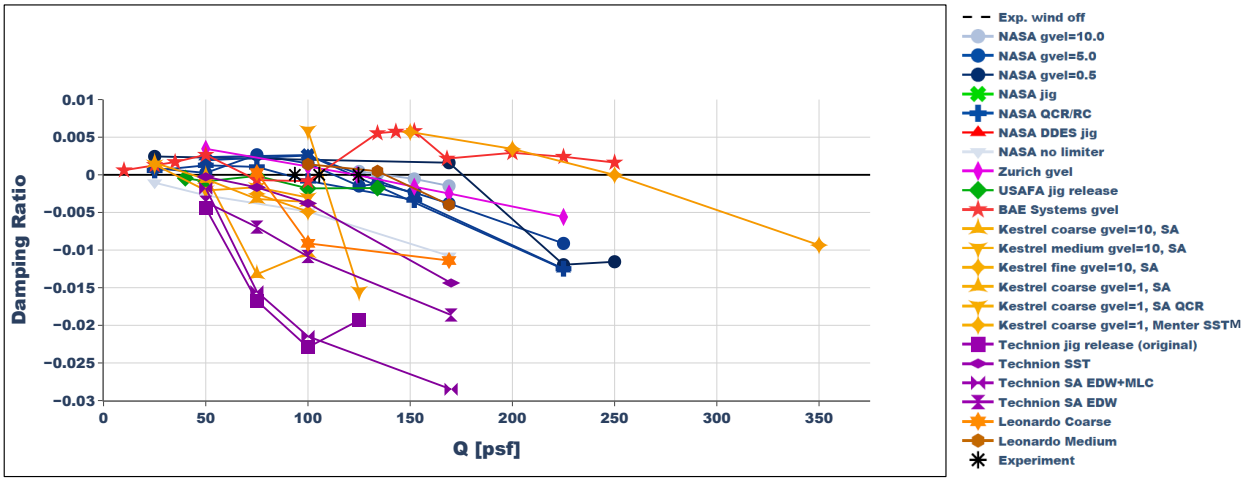

Fig. 4 Damping of the primary component of the pitch response: all teams.

the computational tools are not capable of consistently predicting this case. However, when the results are analyzed in more detail, there are encouraging trends in the computations. The frequencies in Figure 3 are consistent and near the wind-off frequency for low dynamic pressure indicating a pitch-dominated flutter mechanism as reported in the experiment. In Figure 4, many of the predictions are close to zero-damping neutral axis over a range of 25 psf to 150 psf. These very shallow curves indicate a soft flutter crossing and are likely the source of the spread of the three experimental flutter dynamic pressures, which also show that this condition is highly sensitive.

Both Kestrel (see subsection IV.F below) and FUN3D were run with multiple perturbation sizes, and both indicated that the stability of the system at a given dynamic pressure is a function of the amplitude. Understanding this nonlinearity in the responses may be important in future assessments in order to be able to compare results across codes and experiments where perturbation sizes and types of perturbations are not consistent.

As part of verification and validation efforts for transonic flutter, it is important to perform both code-to-code comparisons and code-to-experiment comparisons. More experimental data is needed to properly assess how well the computations predict the experiment. There is a 25% difference between the highest and lowest experimental dynamic pressures, but there are not enough samples to have a rigorous statistical assessment of the true value and uncertainty. Given the sensitivity of the flutter dynamic pressure, other less sensitive measurements need to be collected in future wind tunnel experiments for the validation process, such as the surface pressures and shock location and motion from pressure sensitive paint or time histories of motion.

Further validation against the experiment may require detailed assessment of the simplifications made for the computations. In particular, the computations are performed with zero structural damping and assume the wing in free air with a symmetry plane at the wing root as opposed to being mounted on the splitter plate in the wind tunnel. While zero structural damping is often assumed to make computational predictions more conservative, measured structural damping should be straightforward to include in the model and will have a significant effect on the predicted stability characteristics due to the soft flutter mechanism [18]. Initial computations that include the splitter plate show a juncture flow separation at the root of the wing that affects the shock location on the wing, a strong driver of the aeroelastic stability. Therefore, including the splitter plate and possibly the wind tunnel test section may be required to compare well to the experiment. However, performing a rigorous spatial and temporal convergence with the wing alone is already cost prohibitive for the workshop participants, so this additional complexity is not possible in the near term.

Grounding the computations in experiment is important, but there is much to learn from code-to-code comparisons as well. As previously stated, the majority of the computations qualitatively show the same trends in frequency and damping versus dynamic pressure; however, no two codes show more rigorous quantitative agreement. Questions such as "Is unsteady Reynolds-averaged Navier-Stokes (uRANS) sufficient for this case?" or "Do the predictions made with different types of perturbations agree?" cannot be answered yet. While some participants did perform computations for multiple mesh refinement levels, no participant has been able to demonstrate complete spatial and temporal independence of their results due to the computational cost required to do so. But without this, it is not clear if the differences in predicted response among the computations are due to turbulence modeling choices or discretization error, or some other source. Quantitative agreement across codes would increase confidence in the predictions and conclusions about modeling choices; however, the community is not yet able to achieve this for the transonic high angle of attack condition. In future workshops, an effort among participants to reduce the variation of modeling choices may help improve the agreement among the codes. Future workshop activities should also include developing a better understanding of the physics of transonic stall flutter, and how best to define the problem, and how best to compare results for these predictions.

The objective of the AePW workshop series is to define and to push the state-of-the-art in computational aeroelasticity. The goal of the HAWG is to focus this objective on transonic flutter and shock buffet. While the above questions cannot be answered yet, attempts were made, with mixed results, to use scaled-resolved methods in flutter computations. Note, for example, that NASA's DDES computational results (see subsection IV.A below) presented in the frequency plot, Figure 3, are clearly an outlier and do not show a reduction in frequency as dynamic pressure increases. The presence of the fully separated flow, and/or mixed attached and separated flow together with the moving or deforming body is computationally challenging. Development of Reduced Order Model (ROM) and Linearized Frequency-Domain (LFD) methods is promising but these methods also suffer from complications due to separated flow, and more research is required. Each reader of this report is challenged to answer the question 'what is the state-of-the-art in computational aeroelasticity?' and to share the answer with the community by participating in future AePWs.

IV. Contributing teams to flutter analyses

The flutter results from all seven teams in terms of damping ratio and frequency, are presented in Figure 3 and Figure 4. In the following subsections, each team describes their path to compute flutter q and flutter frequency. Each subsection ends with the plot of that team's flutter prediction using the same color scheme and the same scale as in Figure 3 and Figure 4.

A. NASA Langley–Aeroelasticity Branch

Solutions to the Reynolds-averaged Navier-Stokes (RANS) equations were computed using the FUN3D unstructured finite-volume node-centered flow solver with turbulence closure obtained using the "standard" Spalart-Allmaras (SA) one-equation model. A separate set of results was also obtained with SA turbulence model and with the Quadratic Constitutive Relationship (QCR) 2000 version and the rotation/curvature correction. The FUN3D flow solver is also used with the Delayed Detached Eddy Simulation (DDES) to obtain solutions. The flux limitation was accomplished with and without the Venkatakrishnan limiter, and inviscid fluxes were computed using the Roe scheme [19].

Dynamic analyses of the BSCW configuration requires unsteady-flow analysis. For unsteady-flow analysis, the FUN3D solver utilizes the dual-time-stepping method, which is widely used in CFD. This method involves adding a pseudo-time derivative of the conserved variables to the physical time derivative that appears in the time-dependent Navier-Stokes equations, in much the same way that an artificial time term is often added to the steady Navier-Stokes equations to facilitate an iterative solution to a steady state. Iteratively advancing each time step in pseudo-time allows errors introduced by the linearization of the nonlinear residual to be reduced to zero, assuming the iterations in pseudo-time are fully converged. An additional advantage of the pseudo-time term is that it enhances the diagonal dominance of the linear system, increasing robustness and allowing larger physical time steps to be taken than might otherwise be possible.

Aeroelastic analysis with body-fitted meshes requires a grid deformation capability. The grid deformation in FUN3D is treated as a linear elasticity problem [20]. In this approach, the grid points near the body can move significantly, while the points farther away may not move much. In addition to the moving body capability, the analysis of the BSCW configuration requires a structural dynamics capability. For a dynamic aeroelastic analysis, FUN3D is capable of being loosely coupled with an external finite element solver [21], or in the case of the linear structural dynamics used in this study, an internal modal structural solver can be utilized [20]. This modal solver is formulated and implemented in FUN3D in a manner similar to other NASA Langley aeroelastic codes (CAP-TSD [22] and CFL3D [23]). For the BSCW computations presented here, the structural modes were obtained via a normal modes analysis (solution 103) with the Finite Element Model (FEM) solver MSC Nastran^{TM} [24]. The modes were then interpolated to the surface mesh using the method developed by Samareh [25]. The BSCW FEM is described by Heeg et al. in Ref. [26]. There are two methods implemented in FUN3D for temporal integration of the structural solver. These methods are the Predictor-Corrector (P-C) scheme and the Backward-Difference (BDF) scheme [27]. The presented results use the P-C scheme.

For this study, unstructured grids (meshes) consisting primarily of tetrahedra and prisms that were previously prepared for the first two workshops were used. Based on the AePW gridding guidelines [28], three grids belonging to the same family were then constructed: one with 3 million nodes, one with 9 million nodes, and one with 27 million nodes. In addition, an extra fine mesh was generated with 99 million nodes. These grids and the corresponding FUN3D solutions are referred to as 'coarse', 'medium', 'fine', and 'xfine' respectively. In this paper, only the coarse, fine, and xfine grids were used to generate FUN3D flutter results. The resulting three grid distributions for both the surface and the plane of symmetry are presented in Figure 5.

The BSCW dynamic analyses were performed in a multistep process. First, the steady CFD solution was obtained on the rigid body. Two paths were taken next to obtain the dynamic aeroelastic flutter solution. In the first path, a static aeroelastic solution was obtained by restarting the CFD analysis from the rigid-steady solution in a time-accurate mode with a structural modal solver, allowing the grid to deform. A high value of structural damping ratio (0.9999) was used so the structure could find its equilibrium position with respect to the mean flow before the dynamic response was started. Finally, the flutter solution was restarted from the static aeroelastic solution by setting the structural damping value to zero and providing an initial excitation 'kick' in the form of the generalized velocity. The effects of that initial excitation on the flutter solution are described later. In the second path, the dynamic aeroelastic solution, or a flutter solution, was obtained by skipping the static aeroelastic step and starting the flutter solution directly from the rigid body solution, also referred to as a 'jig shape.'

The effect of that initial kick on the flutter solution is significant. As seen in Figure 6, the initial kick value between

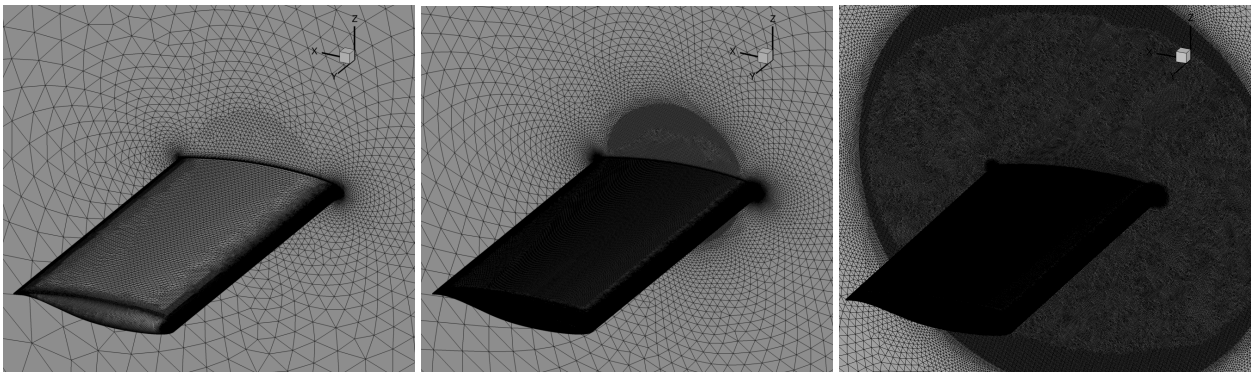

(a) Coarse grid, 3 million nodes. (b) Fine grid, 27 million nodes. (c) Xfine grid, 99 million nodes.

Fig. 5 Coarse, Fine, and Xfine grids.

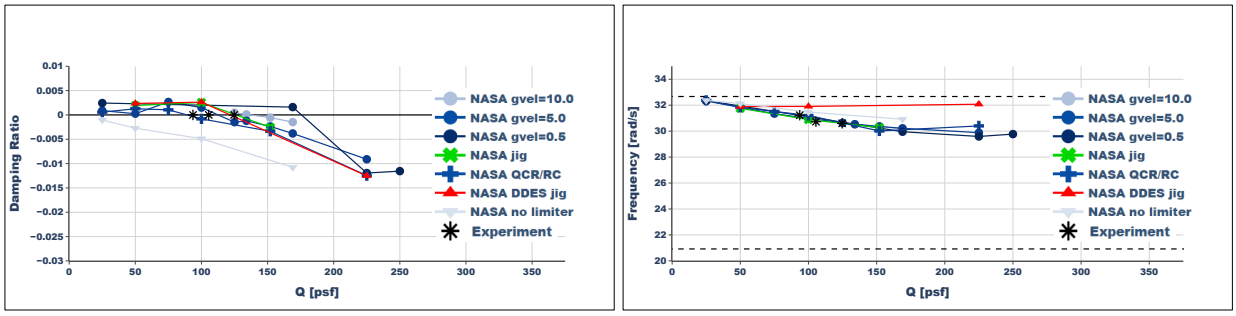

(a) Damping Ratio. (b) Frequency.

Fig. 6 FUN3D results: Damping Ratio and Frequency.

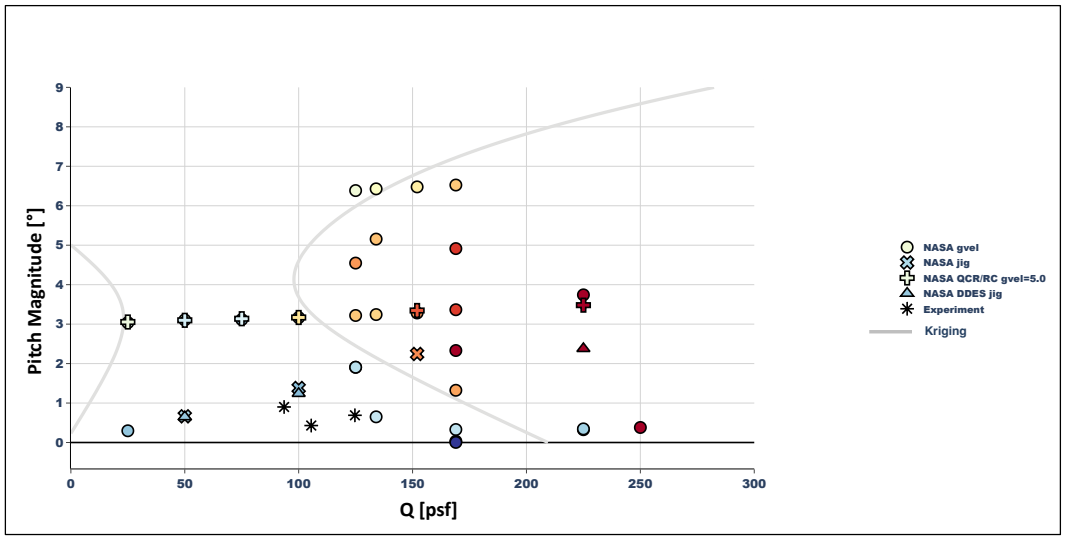

Fig. 7 Kriging-interpolation model.

0.5 and 10, give the range of the computed flutter dynamic pressure between 120 psf and 175 psf. Since FUN3D RANS results do show a dependence on amplitude of the generalized velocity perturbation, a Kriging-interpolation model [29] was fitted through the data to estimate common dynamic behavior, Figure 7. A detailed study of the kick effect on the flutter q is currently underway and results will be published in the future.

The FUN3D flutter solution without applying the flux limiter deserves more attention. This is because the wing

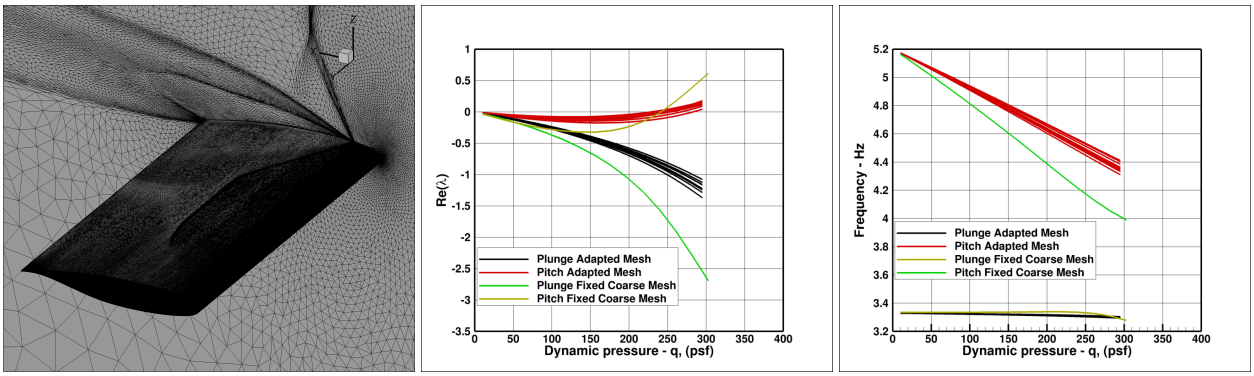

(a) Adapted mesh. **(b) Damping.** **(c) Frequency.**

Fig. 8 FUN3D LFD solution.

response in these solutions is always unstable and a flutter q does not exist. Finally, the damping ratio values computed from the DDES solutions are close to those computed using unsteady RANS. However, the computed flutter frequency is an outlier and requires further attention.

Flutter solutions via the URANS equations described above are most commonly obtained with time-integration, but an alternative workflow is the LFD method [30]. This scheme, which has recently been implemented around a Stabilized Finite Element (SFE) solver embedded within the FUN3D software, involves infinitesimal oscillatory perturbations about a converged steady-state flow solution. A complex-valued linear system of equations is computed for each mode shape (oscillatory surface motion input) and frequency of interest; the resulting complex-valued oscillatory flow fields can be used to calculate a set of generalized aerodynamic forces (GAFs). These GAFs are identical in form to those output from a 'classical' linear aeroelastic analysis built on the doublet lattice method, and they may be used to directly solve for the flutter dynamic pressure via a p-k eigen-analysis. The LFD results that will be shown in this paper have been computed within a mesh adaptation workflow with mesh adaptation mechanics handled via *refine*. The adaptations reduce spatial interpolation error in the flow field based on some scalar field, which for this work is Mach number. For LFD, flow snapshots are constructed using a harmonic perturbation.

The real part of the eigenvalue, representing exponential growth rate, and the corresponding frequency are plotted in Figures 8b and 8c, respectively. The red color represents all the pitch mode solutions and the black color all the plunge mode solutions during the adaptation process. Note that the starting dynamic pressure is always changed to the previously computed flutter q at each adaptation run. The green curves represent a fixed (coarse) mesh solution using SFE at q = 240 psf. Because of the presence of the separated flow, the mesh adaptation at these flow conditions never locks-in on a single adapted-mesh and shows a range of the flutter q between 225 to 280 psf. The wing surface and the plane of symmetry mesh from one of the adaptation cycles near the end of simulation is shown if Figure 8a. These results compare quite well with the results presented by the BAE team in section IV.D below. The BAE team predicts flutter q in the range of 253 to 303 psf.

B. Technion

Aeroelastic simulations for the Technion were conducted using the EZAir flow solver [31]. EZAir is a finite volume, structured, multizone, multiblock Euler/Navier–Stokes solver developed by the Israeli CFD Center. Unsteady Reynolds-averaged Navier-Stokes simulations were conducted using the second order in space Harten, Lax, and van-Leer approximated Riemann solver scheme with contact discontinuity treatment (HLLC).

The wing mesh is of a C-O type, with $126 \times 361 \times 184$ grid points in the spanwise, chordwise, and perpendicular directions. The first grid cell is located at $1 \cdot 10^{-6}$ m from the wing surface. The resulting normalized wall distance is $y^+ \approx 0.5$ for the simulated flow conditions.

Flutter was simulated using three different turbulence models: Spalart–Allmaras (SA) model with Edward and Chandra's modification (EDW) [32] and the mixing layer correction (MLC) [33], k-ω SST [34], and the SA model with the EDW modification (without MLC).

Aeroelastic simulations were restarted from both time-accurate (in which buffet was allowed to develop) and steady-state solutions, with initial conditions of zero modal displacements and velocities. In this way, the initial driver of

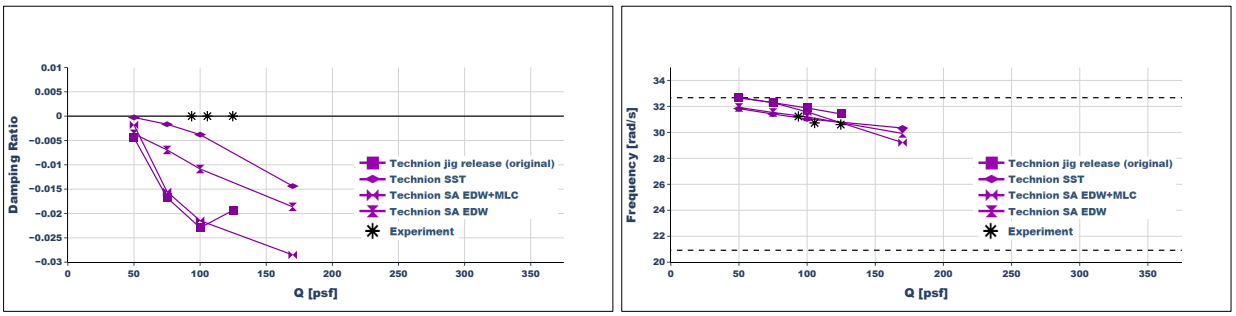

(a) Damping. **(b) Frequency.**

Fig. 9 Technion results: Damping Ratio and Frequency.

the aeroelastic motion was the aerodynamic loading on the fixed (rigid) wing. The aeroelastic simulation was performed in modal coordinates within the flow solver [35], with the wing's deformations under external loads described as a linear combination of the heave and pitch modes. The structural modes were mapped to the computational surface mesh by an Infinite Plate Spline routine [36] embedded within the flow solver, assuming small displacements. For dynamic aeroelastic simulations, a time-accurate scheme, using the dual-time stepping method with a time step of $1 \cdot 10^{-4}$ s and a maximum of 50 sub-iterations was adopted, in which the incremental generalized forces and displacements are computed at each time step. The latter are mapped to the surface mesh and the entire volume grid [35].

The details of the BSCW buffet study and the responses to prescribed modal motion at buffet conditions (Mach 0.8, 5 degrees AoA, and various dynamic pressure values) are presented in Ref. [37]. They indicate that while the pitch motion quenches the buffet itself, the aerodynamic moment coefficient associated with the pitching motion at these conditions results in a pitching moment that leads the motion, and a net positive work done by the aerodynamic forces over a cycle. This is the driver of the stall flutter, dominated by the pitch degree of freedom (DOF), which was observed in the test and simulations at the transonic conditions of Mach 0.8, 5 degrees AoA.

The simulated responses indicate that the MLC correction, which was necessary to capture the buffet unsteadiness at the examined flow conditions (Mach 0.8, 5 degrees AoA), leads to diverging aeroelastic responses at all simulated dynamic pressures. That is, with the MLC correction, the flow separation generates positive aerodynamic work over a cycle, leading to stall flutter, independent of the dynamic pressure.

Considering the SA+EDW and k-ω SST turbulence models, the diverging rate is significantly reduced and, specifically for the k-ω SST model, at a dynamic pressure of 100 psf (at which flutter onset was observed in the test), the simulated responses are almost harmonic, with a tiny negative damping value. A detailed study of the BSCW flutter and its dependency on modeling parameters is presented in Ref. [7]. The computed flutter results are presented in Figure 9.

C. USAFA

Loci/CHEM is a CFD solver developed at the Mississippi State University by Luke et al. [38, 39]. It uses a finite volume scheme with inviscid fluxes calculated using the HLLC inviscid flux scheme by Torro [40]. A low dissipation upwind scheme is also available. The time integration scheme uses a second order Newton implicit scheme. The solver can be used with moving, deforming and overset meshes.

The solver uses a rule-based programming framework called Loci [41–45]. This Loci based solver consists of a set of rules, which are scheduled in the Loci framework during execution. Loci takes care of scheduling as well as MPI partitioning and data transfer. This approach simplifies the design of high-performance parallel codes. The coding is written in the Loci language that, during compilation, is converted into C++ code and compiled to an executable.

The simulations are performed as unsteady RANS/LES simulations based on the SST $k-\omega$ turbulence model. The time step is $\Delta t = 1 \times 10^{-5}$ seconds, which results in a non-dimensional time step of $\Delta t^* \approx 0.005$. We use 5 Newton subiterations in each time step to converge the solution on the moving mesh.

The computational mesh was generated in Pointwise and contains around 12.5 million cells. It has a prism layer on the surface of the wing and prism and tetrahedral cells in the remainder of the computational volume. The symmetry plane used symmetry boundary conditions,generalized which may potentially affect the results at high AoA. In the wind tunnel, the symmetry plane is enforced by a splitter plate; the boundary layer on the splitter plate interacts with the boundary layer on the wing and, at high angles of attack, forms a corner vortex. By using the symmetry boundary

condition we eliminate the boundary layer on the splitter plate and its interaction with the flow around the wing. The computed flutter results are presented in Figure 10.

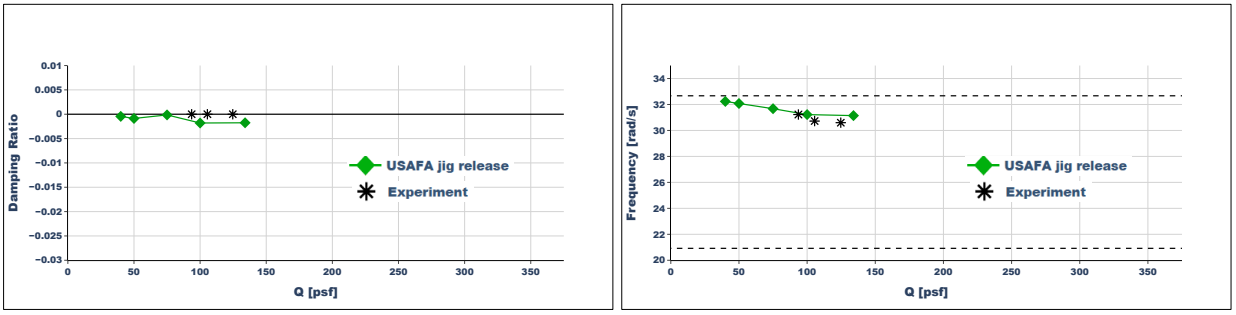

(a) Damping. **(b) Frequency.**

Fig. 10 USAFA results: Damping Ratio and Frequency.

D. BAE Systems Air

This section provides a brief description of the numerical methods and their software implementation used at BAE Systems to produce the results shown in this paper. Full details on the methods and the whole set of results are given in [9].

Simulations were performed using the BAE Systems Corporate CFD Suite, known as Solar and Flare, which includes a mesh generator, CFD solver and an aeroelastic toolkit. The aeroelastic toolkit is composed of a mode shape mapping utility, a Computational Structural Mechanics (CSM) solver as well as a Linearized Frequency Domain (LFD) solver. Regarding the CFD solver, a cell-centered, finite-volume approach is used to integrate the fluid equations for inviscid or viscous flows. A fully implicit scheme is employed for steady-state computations and for the inner iterations of unsteady loops. Time integration is performed with a high order Runge-Kutta scheme. The CSM solver used for this work is based on the modal decomposition of structural deformations and the structural equations are integrated with one of the following schemes: β-Newmark, HHT-α and linear acceleration. The CSM solver can take into account external forces such as gravity and aerodynamics. The latter are projected on the modal shapes to obtain the generalized aerodynamic forces (GAFs) used for the time-integration of the structural equations. The coupling between the CFD and the CSM solver is performed at each time-step (loosely-coupled approach) with the possibility of running multiple CSM inner iterations (strongly-coupled approach). For this work a strongly-coupled approach with a time-step of 0.0002 sec and 2 sub-iterations was adopted.

The aerodynamic loads coming from the CFD solver are used by the CSM solver to compute the up-to-date values of the generalized coordinates. The deformation of the CFD surface mesh is the linear combination of the mode shapes scaled by their corresponding generalized coordinate. Volume mesh deformation is performed with Radial Basis Function (RBF) interpolation unless a set of rigid transformations is specified. For this work, volume deformation is not performed since the 2 d.o.f. are modeled with a rigid translation (plunge mode) and a rigid rotation (pitch mode). Note, although the structure is modeled linearly, nonlinear phenomena such as the interaction between shock wave and boundary layer are fully captured by CFD. The coupled model described so far is referred to as non-linear CFD-CSM. Besides unsteady simulations, the tool can compute the equilibrium solution at steady-state (i.e., trimmed or jig shape) and such steady solutions can be reused to restart unsteady simulations.

To identify the flutter point with the CFD-CSM, a two-step procedure is required. Firstly, an unsteady simulation is restarted from the trimmed steady-state solution. At the beginning of the simulation an initial disturbance of 0.1% of the free-stream velocity is prescribed in the generalized velocity of the modes to enhance any instability of the system. Second, when the simulation is finished, the resulting time-histories of the generalized coordinates are post-processed with either of the logarithmic-decrement (log-dec) or matrix-pencil method to compute the damping. A converging/neutral/diverging time-history corresponds to a positive/zero/negative damping value, respectively, with a diverging curve hinting at the presence of flutter. When results from multiple initial disturbance analyses are available, the damping value can be computed for each simulation. The zero damping condition is then easily found by interpolation. The computed flutter results are presented in Figure 11.

Integrating the CFD-CSM equations in time-domain can be computationally expensive for real-world models. An

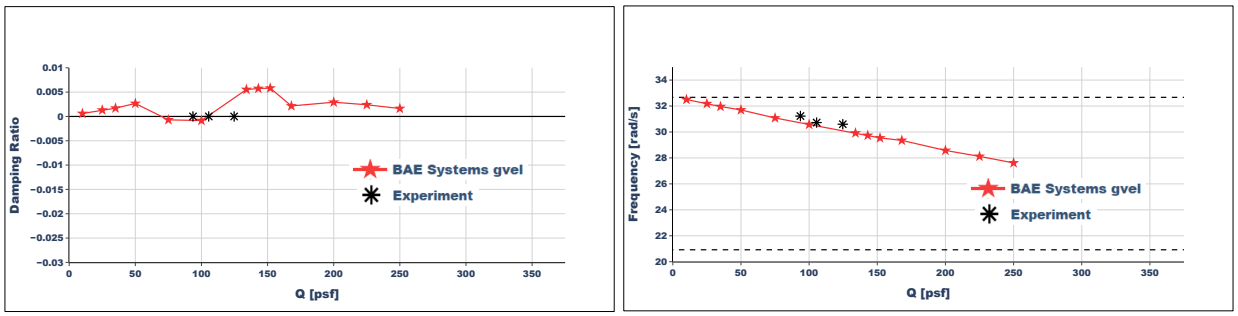

(a) Damping. **(b) Frequency.**

Fig. 11 BAE results: Damping Ratio and Frequency.

alternative to reduce the computational cost is to solve the small-sized flutter problem in frequency-domain with the P-K method and use linearized methods to model the interaction between fluid and structure. Specifically, the flutter equation to solve is

$$\left(M\lambda^2 + K + C\lambda - Q\right)\hat{\mathbf{w}}_s = 0 \tag{2}$$

where $\hat{\mathbf{w}}_s$ is the complex-valued vector containing the structural unknowns, λ is the eigenvalue of the system and M, K, C are the modal mass, stiffness and damping matrices. The matrix Q is the interaction matrix that relates the generalized aerodynamic forces to the structural d.o.f. Computing Q is the computationally expensive part of the linearized methods. To compute the interaction matrix Q, the pulse excitation method can be used. Starting from an equilibrium condition, a forced-motion unsteady CFD-CSM simulation is performed for each structural degree-of-freedom. The parameters which define the excitation shape and the simulation settings are related to the frequency range of interest. One time-domain simulation is needed for each generalized coordinate, thus exciting one structural DOF at time.

An additional drift simulation (i.e. with a non-moving structure) is optionally performed to take into account any deviation of generalized forces from their equilibrium values. Once ready, the time-histories of the generalized forces are post-processed. From each pulse excitation simulation, one corresponding row in the interaction matrix Q is computed with a Discrete Fourier Transformation. An alternative method for the computation of Q is the LFD solver. An equilibrium condition is identified for which the non-linear, residual function of the aerodynamic equations is approximately zero. This is usually the result of a steady-state simulation. The CFD-CSM solver is then linearized around this equilibrium condition using automatic differentiation and the equations are rewritten in frequency-domain by assuming a harmonic motion for both fluid and structural unknowns. The arising linear system is solved once for each structural DOF and the complex-valued solution, in turns, enables the computation of the interaction matrix Q.

1. Results

The steady-state solution needed to perform the flow linearization was obtained with a static aeroelastic trimming. In practice, a steady-state coupled CFD-CSM simulation was run with the SA turbulence model. Every 500 CFD iterations, one coupled CFD-CSM iteration was performed to update the wing position in terms of heave translation and pitch rotation. An artificial damping of $250Ns/m$ was added to the structural model to speed-up the trimming process, which converged in less than 80 coupled CFD-CSM iterations. Two results were obtained: the equilibrium position of the wing (i.e., non-zero vertical translation and non-zero pitch rotation) and the corresponding flow solution. The LFD solver was then restarted from the aeroelastic trimmed solution and the dynamic derivatives were computed at 8 frequencies, specifically 0 rad/ s, 5 rad/ s, 10 rad/ s, 15 rad/ s, 20 rad/ s, 30 rad/ s, 45 rad/ s and 60 rad/ s.

Although the LFD needs only one linearization point, the whole process was repeated for two flow conditions labeled as 'Case 5' and 'Case 6' (*Case 5* at $q = 75$ psf and *Case 6* at $q = 100$ psf, see Fig. 12). The objective was to investigate the effects of the linearization point on the dynamic derivatives and the evaluation of the flutter point. Once the entries of the matrix Q are available, the flutter Eq. (2) can be solved with a tracing algorithm based on Newton's method [46]. As a result, the evolution of the two eigenvalues (one for each DOF) of Eq. (2) is shown in Fig. 12 with respect to the dynamic pressure.

The heave mode is always stable as visible in Fig. 12a. Conversely, the pitch mode evolves into flutter when a critical value of dynamic pressure q^* is reached. The specific value of q^* depends on the flow condition at which the dynamic

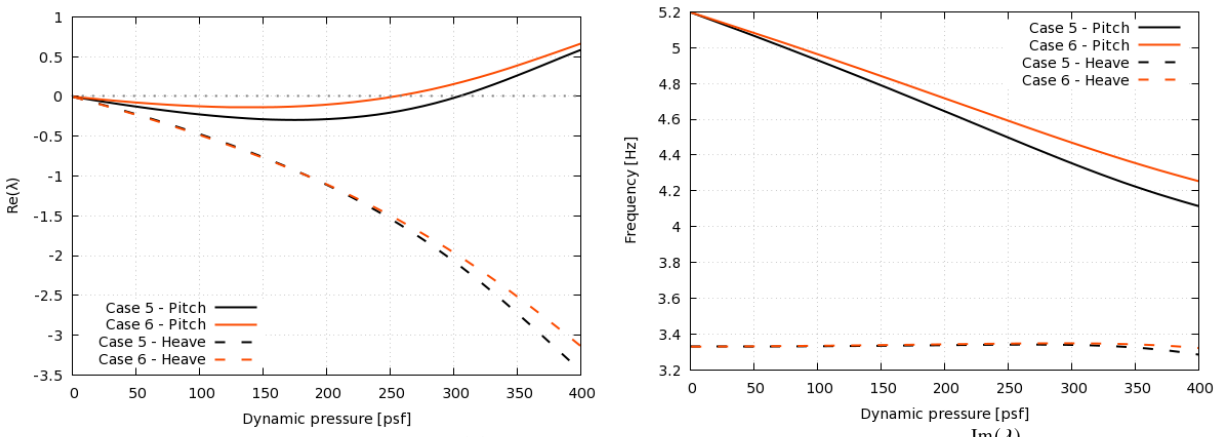

(a) Real part of the eigenvalue, Re (λ) **(b) Frequency,** $\frac{\text{Im}(\lambda)}{2\pi}$

Fig. 12 Flutter analysis with the LFD method. Plots of the eigenvalues of Eq. (2) with respect to dynamic pressure. The pitch mode becomes unstable at 253 psf **for *Case 6*,** 303 psf **for *Case 5*.**

derivatives were computed. It was found that $q^* = 253$ psf for *Case 6* and $q^* = 303$ psf for *Case 5*. Regarding the flutter frequency in Fig. 12b, the two flow conditions lead to very similar values in the range [4.3,4.6] Hz.

E. Zurich University and University of Southampton

The assessment of linear stability and the dynamic responses for given values of Mach number, angle of attack and dynamic pressure were obtained from time integration of a state-space model with pitch and plunge degrees of freedom using non-linear time-accurate aerodynamic forces from a second-order parametric Reduced Order Model (ROM). The parametric ROM was inspired to the Volterra Series presented in Ref. [47]. First and second order Volterra kernels were identified from time-accurate CFD responses. To this end, we used SU2 v7.5.0 [48] with the one equation Spalart-Allmaras turbulence model. A $1v$ multigrid scheme is adopted for accelerating the convergence of CFD simulations. The Jameson-Schmidt-Turkel, JST, central scheme with artificial dissipation is adopted for the discretization of convective flows. The gradients of the flow variables are calculated using a Green Gauss method. The linear solver biconjugate gradient stabilization is chosen, with ILU preconditioner applied. URANS simulations were all computed by restarting the solution from the steady–state solution. All unsteady simulations were obtained as response to smoothed step pitching input signals, rotating the airfoil around the mid–chord:

$$\alpha(\tau) = \alpha_0 \left(1 - e^{-\tau/\tau_{ref}}\right), \tag{3}$$

where τ_{ref} is chosen to provide a smooth impulsive response. Input signals with different magnitude α_0 were used to separately identify linear and non-linear kernels. Following Ref. [47], the linear ones were identified from a lower amplitude response, whereas the second order ones were identified from the difference between the response to a larger input signal and the response used to identify the linear kernels. Figure 13 compares the larger magnitude responses computed with CFD, with the linear and non-linear approximations.

A mixed-type grid with $15.6 \cdot 10^6$ elements and 130,816 surface elements was generated, structured on the wing surface and in the first layers of the boundary layer, voxel in the rest of the computational domain. A $y^+ = 1$ is adopted, after a preliminary mesh convergence study that ensured an adequate resolution of the boundary layer and shock wave. The computational domain extends 100 chords from the solid wall to the farfield. An impression of the grid can be obtained from Figure 14.

The parametric Reduced Order Model was developed over a (Mach number, angle of attack) space, in the ranges of [0,5] and [0.70,0.84] degrees, respectively. These ranges were selected in order to capture linear and non-linear physics. In practice, the Volterra kernels were identified independently for n samples in the parameters space. Subsequently, we trained an artificial neural network with the n samples and used it to reconstruct the Volterra kernels over the entire parameter space. It is worthwhile mentioning that the kernel reconstruction also provides data regularization. The hyperparameters of the artificial neural network are listed in Table 3. The computed flutter results are presented in Figure 15.

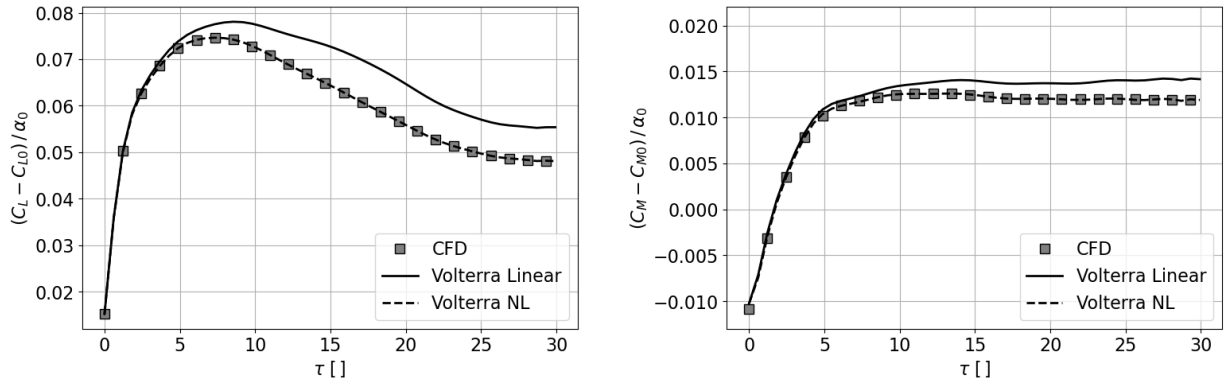

Fig. 13 Aerodynamic loads reconstruction with linear and nonlinear Volterra kernels at $M = 0.829$ and $\alpha_0 = 4.277$ degrees. The response was normalized by the pitch angle input step, after subtracting the steady–state value.

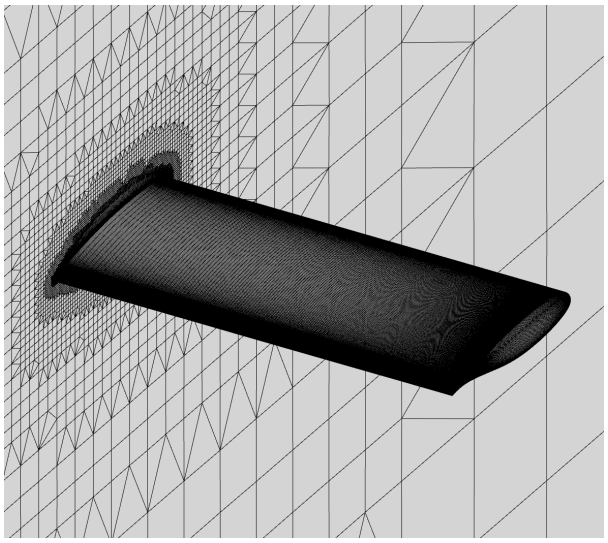

Fig. 14 Impression of the BSCW CFD grid.

Table 3 Optimal hyperparameters for the linear and nonlinear Volterra kernels identification.

Hyperparameter	**Optimal Value**	
	Linear Kernels	NL kernels
Learning rate	10^{-4}	10^{-4}
Number of Hidden Layers	5	7
Activation function	PReLu	PReLu
Number of parameters	144,502	259,890

F. CREATE-AV, Kestrel

Kestrel's multi-physics coupling capabilities require all the physics solvers that are coupling to operate in the time domain. The following generic approach is used to approximate the dynamic pressure of flutter onset for a given Mach number using time-domain solvers.

1) Select the starting point freestream conditions, normally by specifying angle of attack, angle of sideslip, Mach number, density, and dynamic pressure.

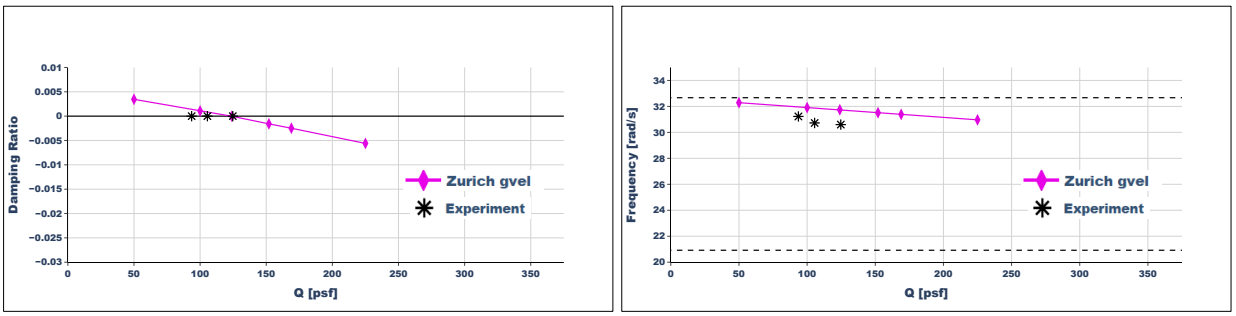

(a) Damping. **(b) Frequency.**

Fig. 15 Zurich University and University of Southampton results: Damping ratio and Frequency.

2) Converge the flow field around a non-moving, non-deforming grid at these flow conditions.
3) Using step 2) as a starting point, find the aeroelastic equilibrium condition for this flow condition by running a moving and/or deforming simulation with a significant amount of structural damping.
4) Using step 3) as a starting point, simulate the dynamic response at these flow conditions by generating an initial perturbation from the aeroelastic equilibrium and allowing both the fluid solver and the structural solver to solve time-accurately, without the excessive damping added to step 3).
5) Look at one or more output quantities from the dynamic response, often one or more mode amplitudes, or sometimes the physical displacement of one or more points on the geometry. Evaluate if these signals are amplifying or decaying over time. An amplifying signal indicates this quantity is unstable at this flow condition, and a decaying signal indicates this quantity is stable at this flow condition.
6) Change the dynamic pressure and return to step 2). If this flow condition is stable, then the dynamic pressure should be increased. If this flow condition is unstable, then the dynamic pressure should be decreased.
7) Continue until the flutter onset dynamic pressure, or the dynamic pressure at which the response changes from stable to unstable, is bounded.

For the simulations reported on in this paper, for steps 2)-4), Kestrel's KCFD flow solver will provide the flow solution and Kestrel's ModalSD structural dynamics solver will provide the structural dynamics response. For step 5), a signal processing technique known as the matrix pencil method will compute a damping ratio for each signal [16], where negative damping ratios indicate an unstable signal and positive damping ratios indicate a decaying signal.

1. Grids

The CREATE-AV team simulations make use of the unstructured fluid grids provided on the AePW-2 website [28]. This is a family of meshes containing mostly prism and tetrahedral cells, with the near-wall cell spacing generated with a cell-centered solver in mind. The "coarse" mesh contains 3.6 million cells, the "medium" mesh contains 11.6 million cells, and the "fine" mesh contains 36.0 million cells. Fig. 16 shows the upper surface of the wing and a portion of the symmetry plane for each of these meshes. All three meshes are used as-is, apart from converting them from the provided format into the AVM format needed by Kestrel's flow solvers.

The CREATE-AV team simulations make use of the MSC Nastran solution generated in [26], which is also available on the AePW-2 website. This solution is converted into a modal model for use in Kestrel's ModalSD solver. The original MSC Nastran model contains a flat plate to represent the wing and a spring at the wing root to represent the pitch and plunge apparatus (PAPA). The model has a first mode with a frequency of 3.329873 Hz associated with the plunge of the PAPA, and a second mode with a frequency of 5.199601 Hz associated with the pitch of the PAPA. The first mode associated with the deformation of the wing itself has a frequency of 126.9232 Hz and is associated with the first bending mode. The CREATE-AV team simulations include both the PAPA modes and the eighteen wing modes that are in the MSC Nastran solution, but in all of the simulations only the PAPA modes exhibit activity.

2. Structural Solver, Multi-Physics Coupling, and Fluid Volume Mesh Deformation

The CREATE-AV team simulations make use of ModalSD, which is Kestrel's second-order modal structural dynamics solver [49]. ModalSD uses a sub-iteration scheme similar to that used in KCFD in order to support sub-iteration data transfer between solvers if the user requests it. ModalSD also has a predictor-corrector time integration

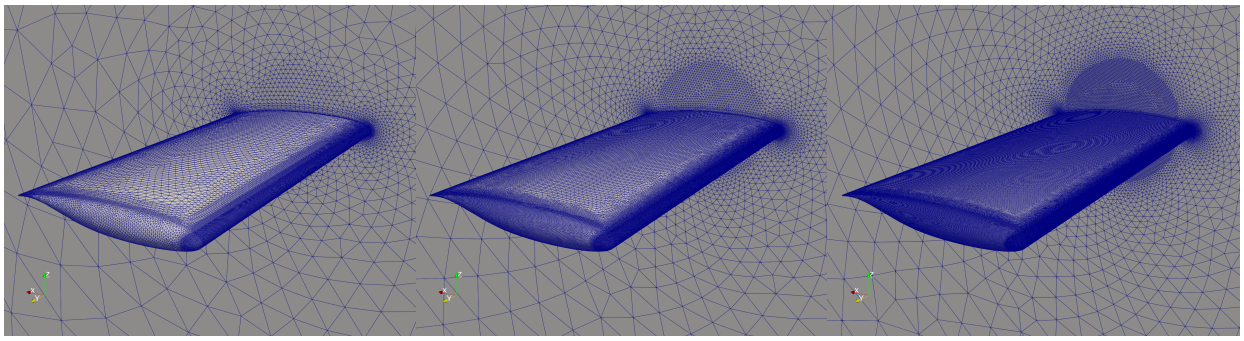

(a) coarse mesh **(b) medium mesh** **(c) fine mesh**

Fig. 16 Fluid meshes.

scheme, which is the default scheme. Kestrel uses its own format for specifying the modal model but provides tools for converting eigenvalue solutions from Nastran and Sierra/SD structural dynamics solvers.

The forces are interpolated from the fluid mesh to the structural model and the displacements are interpolated from the structural model to the fluid surface using global splines similar to those found in the ZAERO tool from ZONA Technology, Inc. [50]. There are four methods available for the information transfer in Kestrel: a rigid-body attachment, a beam spline, an infinite plate spline, and a thin plate spline. The user tells Kestrel which structural nodes should be mapped to which fluid surface patches, and Kestrel then determines the topology of those structural nodes and chooses the most appropriate of the spline methods.

Kestrel supports several schemes to control the temporal accuracy of coupled aeroelastic simulations [49, 51]. Both the fluid and structural solvers can take multiple time steps without exchanging information with each other, which is bad for time-accuracy but can improve the efficiency of simulations seeking aeroelastic equilibrium in a steady flow field. Conversely, the fluid and structural solvers can exchange information every time step. When the structural solvers use a predictor-corrector scheme this results in a second-order coupled solution, otherwise it results in a "first-order" lagged solution. Finally, Kestrel can exchange information during each sub-iteration of the fluid and modal structural solver solution process, also resulting in a second-order coupled solution.

After the fluid surface mesh is updated by the interpolated displacements, the fluid volume mesh must be corrected to accommodate the moved surface nodes. Kestrel makes use of a two-stage approach to deform the volume mesh [52]. The first stage moves the nodes close to the deformed surface as "rigidly" as possible, and the second stage uses a surface influence scheme to relax the deformation into the volume. This approach is algebraic and has the advantage that the location of each node in the volume mesh is a function of the initial mesh and the current deformed surface mesh and does not depend on the mesh deformation history.

The CREATE-AV team simulations make use of the infinite-plate spline and the predictor-corrector time coupling. The computed flutter results are presented in Figure 17.

More results, and a more detailed discussion of these results, are available in Ref. [8].

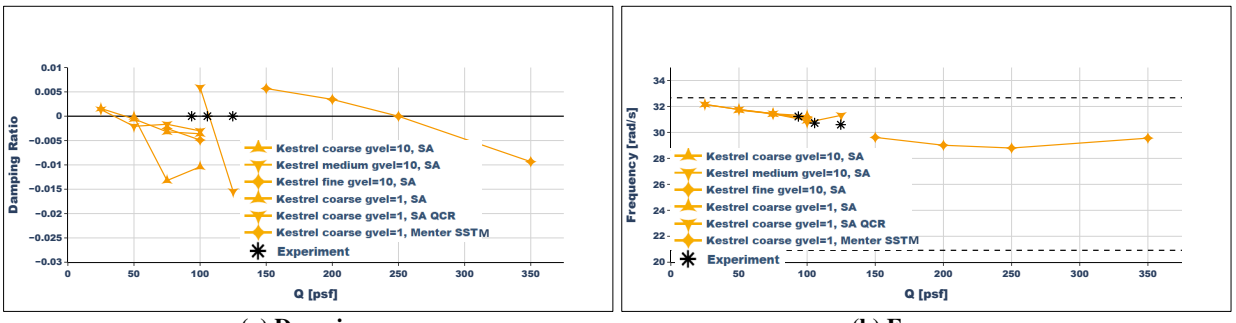

(a) Damping. **(b) Frequency.**

Fig. 17 CREATE-AV, Kestrel results: Damping ratio and Frequency.

G. Leonardo Labs

The aeroelastic simulations were carried out using a partitioned technique for the fluid-structure coupling. Opposed to the monolithic coupling, the partitioned approach offers several advantages, since it links existing software on a higher level, benefiting from higher flexibility and lower time-to-solution, without any significant implementation effort. For the BSCW simulations, the open-source preCICE [53] library was employed for the coupling. This library has proven able to exploit efficiently HPC infrastructures for several types of interface coupling, including fluid-structure interaction.

All the simulations were conducted on 4 CPU nodes of the davinci-1 supercomputer, each characterized by 2 Intel(R) Xeon(R) Platinum 8260 CPU (24 cores each). Firstly, rigid stand-alone CFD simulations were run to obtain a steady-state converged solution. Unsteady aeroelastic calculations were then restarted from this condition using a jig-release approach. Wing pitch and plunge data were extracted during the calculation and used to determine the aerodynamic damping for each simulated condition.

For the fluid component, a custom version of the ICSFoam library developed by Oliani *et al.* [54] was used for the simulation. This library is based on the OpenFOAM CFD framework and allows to solve coupled systems of partial differential equations with the finite volume method on stationary and moving grids. Specifically, an implicit density-based solver was used to solve the unsteady Reynolds-averaged Navier-Stokes equations. The solver was connected to preCICE using the official OpenFOAM adapter developed by Chourdakis *et al.* [55]. The dual time-stepping technique was used to solve the unsteady aeroelastic problem, with a second-order backward discretization in time. The physical time step is $\Delta t = 2.5 \times 10^{-4}$, while local time stepping with 15 subiterations and a CFL of 25 was employed for the inner loop. The linearized system of equations is obtained using a first-order approximation of the system Jacobian and solved using the GMRES linear solver with LUSGS preconditioner. Convective fluxes were computed through the HLLC approximate Riemann solver combined with a MUSCL reconstruction of primitive variables with van Leer limiter to achieve a nominally second-order accurate spatial discretization in space. Viscous fluxes were computed using a standard second-order central scheme. For turbulence modeling, the two-equation k-omega SST mode available in OpenFOAM was selected.

The coarse and medium grids generated by NASA for the workshop were selected for the simulation [28]. Specifically, the grids had 3.6 and 11.6 million elements, respectively. A free stream boundary condition was set at the farfield boundaries, while a no-slip condition was enforced on the wing walls. Finally, a symmetry condition was used on the plane corresponding to the wing root.

Radial Basis Functions (RBF) were used to accommodate grid displacements caused by wing oscillations. For this purpose, the *RBFMeshMotionSolver* library included in the solids4Foam project [56] was employed. Although computationally cumbersome, the use of RBF allowed to preserve the grid quality throughout the mesh oscillation, without impacting the stability of the simulation. To reduce the computational cost of the RBF solver, a coarsening was applied to the number of surface points used as reference for the RBF motion. A total of 100 points were selected in this configuration.

The open-source FEM software Calculix was chosen for the structural part. This software supports several functionalities, including implicit static and dynamic solvers, explicit dynamic solvers, and eigenvalue extraction. For the present case, the dynamic solver supplemented with the corresponding preCICE adapter were selected. The mass properties, stiffness properties and pitch rotation axis of the original system were set to match the specifics provided to workshop participants. A simplified model consisting of a rigid body connected to concentrated masses and spring elements was created. The geometry of the wing consisted of 12k surface points connected to a reference point using the CalculiX rigid body feature. Due to the lack of torsional springs in Calculix, the pitch rotation around the y axis is generated by means of two linear springs, respectively connected to additional points (included in the rigid body) and acting in the x direction. The concentrated masses were placed in these two points to achieve the desired translational and rotational inertia of the PAPA structure. The plunge motion was accounted for with a spring acting on the z axis and connected to the reference point. Since the pitch and plunge springs act on different axes, the two modes are effectively decoupled. All the simulations were run using the explicit dynamic solver of Calculix.

For the FSI problem, preCICE explicit coupling scheme was selected. With this kind of scheme, the exchange of data at the interface is performed by transfer of the nodal displacement from the solid solver to the fluid solver, and nodal reaction forces for the other way around. In this particular case, the resolution of the FEM mesh at the interface does not influence the computational size of the problem, since the rigid body feature was used to construct the model. Consequently, it was possible to use a finely discretized interface with a nearest-neighbor mapping scheme. The computed flutter results are presented in Figure 18.

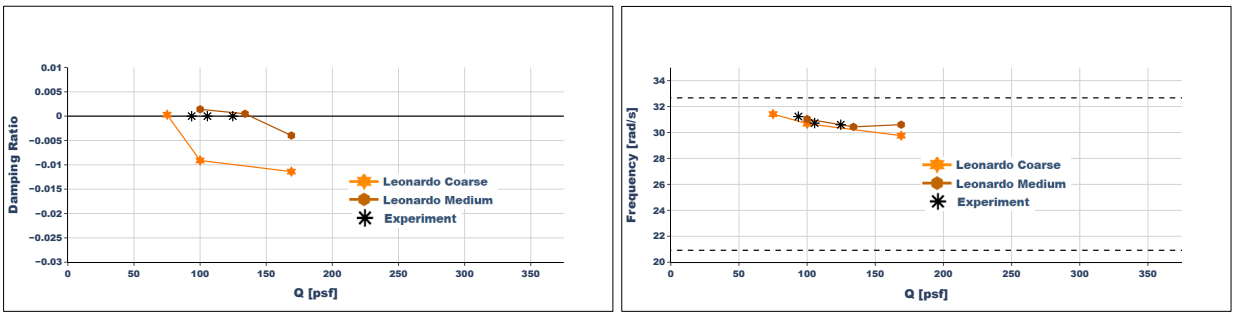

(a) Damping. **(b) Frequency.**

Fig. 18 Leonardo Labs results: Damping ratio and Frequency.

Acknowledgments

The NASA Langley results are supported by the Transformational Tools and Technologies (TTT) project of the NASA Transformative Aeronautics Concepts Program (TACP).

The CREATE-AV team results and discussion are a product of the Computational Research and Engineering for Acquisition Tools and Environments (CREATE) Program sponsored by the U.S. Department of Defense HPC Modernization Program (HPCMP) Office. In addition, the CREATE-AV team would like to acknowledge the support of the supercomputing resources provided by the HPCMP at the Navy DoD Supercomputing Resource Center (DSRC), the Army Engineer Research and Development Center (ERDC) DSRC, and the Air Force Research Laboratory (AFRL) DSRC.

NASA team would like to sincerely thank all the teams in participating in the AePW HAWG activity and in providing flutter results.

References

[1] Heeg, J., Chwalowski, P., Schuster, D. M., Dalenbring, M., Jirasek, A., Taylor, P., Mavriplis, D. J., Boucke, A., Ballmann, J., and Smith, M., "Overview and Lessons Learned from the Aeroelastic Prediction Workshop," IFASD Paper 2013-1A, 2013.

[2] Heeg, J., Wieseman, C. D., and Chwalowski, P., "Data Comparisons and Summary of the Second Aeroelastic Prediction Workshop," AIAA Paper 2016-3121, 2016.

[3] `http://nescacademy.nasa.gov/workshops/AePW3/public/`, 2023.

[4] Chwalowski, P., McHugh, G. R., Massey, S. J., Poplingher, L., Raveh, D. E., Jirasek, A., Seidel, J., Giannelis, N. F., Vio, G. A., Venkatraman, K., Singh, M., Ahrabi, B. R., Hong, M., and Slotnick, J., "Shock-Buffet Prediction Report in Support of the High Angle Working Group at the Third Aeroelastic Prediction Workshop," AIAA Paper 2024, Jan. 2024.

[5] Heeg, J., and Chwalowski, P., "Investigating the Transonic flutter Boundary of the Benchmark Supercritial Wing," AIAA Paper 2017-0191, Jan. 2017.

[6] Heeg, J., and Piatak, D. J., "Experimental data from the Benchmark SuperCritical Wing wind tunnel test on an oscillating turntable," AIAA Paper 2013-1802, Apr. 2013.

[7] Poplingher, L., and Raveh, D. E., "Computational Study of Stall Flutter of the Benchmark Supercritical Wing," *AIAA SciTech 2024 Forum*, 2024.

[8] Lamberson, S. E. J., and Prosser, D., "HPCMP CREATE™-AV Kestrel Flutter Computations for the Third Aeroelastic Prediction Workshop High Angle Working Group," *AIAA Scitech 2024 Forum*, AIAA, 2024.

[9] Pagliuca, G., Berberoff-Naval, J. N., and Forster, M., "Flutter Solution of the NASA Benchmark Supercritical Wing using Linear and Non-Linear Methods," IFASD-2022-028, 2022.

[10] Chwalowski, P., Stanford, B. K., Massey, S. J., McHugh, G. R., and Jacobson, K. E., "Progress on Transonic Flutter and Shock Buffet Computations in Support of the Third Aeroelastic Prediction Workshop," *AIAA SCITECH 2022 Forum*, AIAA, 2022. doi:10.2514/6.2022-1347.

[11] Jirasek, A., and Seidel, J., "Study of Benchmark Super Critical Wing at Mach 0.8," AIAA Paper 2022-0175, Jan. 2022.

[12] Dansberry, B. E., Durham, M. H., Bennett, Rivera, J. A., Silva, W. A., and Wieseaman, C. D., "Experimental Unsteady Pressures at Flutter on the Supercritical Wing Benchmark Model." AIAA Paper 1993-1592-CP, 1993.

[13] Piatak, D. J., and Cleckner, C. S., "A New Forced Oscillation Capability for the Transonic Dynamics Tunnel," AIAA Paper 2002-0171, Jan. 2002.

[14] Schuster, D. M., "Aerodynamic Measurements on a Large Splitter Plate for the NASA Langley Transonic Dynamics Tunnel," NASA TM 2001-210828, Mar. 2001.

[15] Dansberry, B. E., Durham, M. H., Bennett, R. M., Turnock, D. L., Silva, W. A., and Rivera, J. A., "Physical Properties of the Benchmark Models Program Supercritical Wing," NASA Technical Memorandum 4457, 1993.

[16] Kiviaho, J. F., Jacobson, K. E., and Kennedy, G. J., "Flutter Boundary Identification from Time-Domain Simulations Using the Matrix Pencil Method," *AIAA Journal*, Vol. 57, No. 8, 2019, pp. 3639–3645. doi:10.2514/1.J058072, URL https://doi.org/10.2514/1.J058072.

[17] Jacobson, K. E., Kiviaho, J. F., Kennedy, G. J., and Smith, M. J., ""Evaluation of Time-domain Damping Identification Methods for Flutter-constrained Optimization"," *Journal of Fluids and Structures*, Vol. 87, 2019, pp. 174 – 188.

[18] Stanford, B. K., and Jacobson, K. E., "Transonic Aeroelastic Modeling of the NACA 0012 Benchmark Wing," *AIAA Journal*, Vol. 59, No. 10, 2021, pp. 4134–4143. doi:10.2514/1.J060328, URL https://doi.org/10.2514/1.J060328.

[19] "FUN3D 13.7 Manual," URL=https://fun3d.larc.nasa.gov, 2022.

[20] Biedron, R. T., and Thomas, J. L., "Recent Enhancements to the FUN3D Flow Solver for Moving-Mesh Applications," AIAA Paper 2009-1360, Jan. 2009.

[21] Biedron, R. T., and Lee-Rausch, E. M., "Rotor Airloads Prediction Using Unstructured Meshes and Loose CFD/CSD Coupling," AIAA Paper 2008-7341, 2008.

[22] Batina, J. T., Seidel, D. A., Bland, S. R., and Bennet, R. M., "Unsteady Transonic Flow Calculations for Realistic Aircraft Configurations," AIAA Paper 1987-0850, 1987.

[23] Bartels, R. E., Rumsey, C. L., and Biedron, R. T., "CFL3D Version 6.4 - General Usage and Aeroelastic Analysis," NASA TM 2006-214301, Mar. 2006.

[24] *MSC Nastran*, MSC Software, Santa Ana, CA, 2008. http://www.mscsoftware.com/products/msc_nastran.cfm.

[25] Samareh, J. A., "Discrete Data Transfer Technique for Fluid—Structure Interaction," AIAA Paper 2007–4309, Jun. 2007.

[26] Heeg, J., Chwalowski, P., Schuster, D. M., Raveh, D., Jirasek, A., and Dalenbring, M., "Plans and Example Results for the 2^{nd} AIAA Aeroelastic Prediction Workshop," *56^{th} AIAA/ASCE/AHS/ASC Structures, Structural Dynamics, and Materials Conference*, AIAA, 2015. doi:10.2514/6.2015-0437.

[27] Chwalowski, P., Heeg, J., and Biedron, R., "Numerical Investigations of the Benchmark Supercritical Wing in Transonic Flow," AIAA Paper 2017-0190, Jan. 2017.

[28] "Aeroelastic Prediction Workshop-2," URL=http://nescacademy.nasa.gov/workshops/AePW2/public, 2016.

[29] Martins, J. R. R. A., and Ning, A., *Engineering Design Optimization*, Cambridge University Press, ISBN: 9781108833417., 2021.

[30] Jacobson, K. E., Stanford, B. K., Wood, S. L., and Anderson, W. K., "Flutter Analysis with Stabilized Finite Elements based on the Linearized Frequency-domain Approach," AIAA Paper 2020-0403, Jan. 2020.

[31] Kidron, Y., Levy, Y., and Wasserman, M., "The EZAIR CFD Solvers Suite: EZAIR Theoretical and User's Manual - Version 4.59," Tech. Rep. 2020-16, Israeli CFD Center, 2020.

[32] Edwards, J. R., and Chandra, S., "Comparison of Eddy Viscosity-Transport Turbulence Models for Three-Dimensional, Shock-Separated Flowfields," *AIAA Journal*, Vol. 34, 1996, pp. 756–763. doi:10.2514/3.13137.

[33] Spalart, P., "Trends in Turbulence Treatments," *Fluids 2000 Conference and Exhibit*, 2000. doi:10.2514/6.2000-2306, AIAA Paper 2000-2306.

[34] Menter, F., "Zonal Two Equation k-ω Turbulence Models For Aerodynamic Flows," *23rd Fluid Dynamics, Plasmadynamics, and Lasers Conference*, 1993. doi:10.2514/6.1993-2906, AIAA Paper 1993-2906.

[35] Raveh, D. E., Mor Yossef, Y., and Levy, Y., "Analyses for the Second Aeroelastic Prediction Workshop Using the EZNSS Code," *AIAA Journal*, Vol. 56, No. 1, 2018, pp. 387–402. doi:10.2514/1.J055960.

[36] Harder, R. L., and Desmarais, R. N., "Interpolation Using Surface Splines," *Journal of Aircraft*, Vol. 9, No. 2, 1972, pp. 189–191. doi:10.2514/3.44330.

[37] Poplingher, L., and Raveh, D. E., "Shock Buffet and Associated Fluid–Structure Interactions of the Benchmark Supercritical Wing," *AIAA Journal*, Vol. 61, No. 6, 2023, pp. 2381–2399.

[38] Luke, E. D., Tong, X.-L., Wu, J., Tang, L., and Cinnella, P., " CHEM: A Chemically Reacting Flow Solver for Generalized Grids," Tech. rep., AIAA 2003, 2003.

[39] "Chem," URL=http://web.cse.msstate.edu/%7Eluke/chem/index.html, 2019.

[40] Toro, E., Spruce, M., and Speares, M., " Restoration of the contact surface in the HLL-Riemann solver," *Shock Waves*, Vol. 4, 1994, pp. 25–34.

[41] "Loci," URL=http://web.cse.msstate.edu/̃luke/loci/index.html, 2019.

[42] Luke, E., "Loci: A Deductive Framework for Graph-Based Algorithms," *Third International Symposium on Computing in Object-Oriented Parallel Environments*, edited by S. Matsuoka, R. Oldehoeft, and M. Tholburn, Springer-Verlag, 1999, pp. 142–153.

[43] Luke, E. A., Koomullil, R., and Soni, B. K., "Integrated Multidisciplinary Simulation Environment for Analysis and Testing of RBCC Systems," Final report for nasa grant nas13-98033 delivery order #161, Simulation and Design Center, Mississippi State University, 2 Research Blvd, Starkville, MS 39759, June 2003.

[44] Luke, E. A., Tong, X., Wu, J., Tang, L., and Cinnella, P., "A Step Towards 'Shape-Shifting' Algorithms: Reacting Flow Simulations Using Generalized Grids," *Proceedings of the 39th AIAA Aerospace Sciences Meeting and Exhibit*, AIAA, 2001.

[45] Luke, E., and George, T., "Loci: A Rule-Based Framework for Parallel Multidisciplinary Simyulation Synthesis," *Journal of Functional Programming*, Vol. 14, No. 03, 2005, pp. 477–502.

[46] Pagliuca, G., and Timme, S., "Flight Dynamics Mode Identification and Model Reduction using Computational Fluid Dynamics," AIAA-2016-3850, 2016. doi:10.2514/6.2016-3850.

[47] Levin, D., Bastos, K. K., and Dowell, E. H., "Convolution and Volterra Series Approach to Reduced-Order Modeling of Unsteady Aerodynamic Loads," *AIAA Journal*, Vol. 60, No. 3, 2022, pp. 1663–1678.

[48] Economon, T. D., Palacios, F., Copeland, S. R., Lukaczyk, T. W., and Alonso, J. J., "SU2: An open-source suite for multiphysics simulation and design," *Aiaa Journal*, Vol. 54, No. 3, 2016, pp. 828–846.

[49] Lamberson, S. E. J., and Hallissy, B. P., "Aeroelastic Simualtions with Modal and Finite-Element Structural Solvers Using CREATE-AV/Kestrel v5," *53rd AIAA Aerospace Sciences Meeting*, AIAA, 2015. doi:10.2514/6.2015-0041.

[50] *ZAERO Theoretical Manual*, ZONA Technologies, Inc., 8$^{\text{th}}$ ed., 2008.

[51] Lamberson, S. E. J., McDaniel, D. R., and Morton, S. A., "High-Fidelity Aeroelastic Simualtions with HPCMP CREATE™-AV Kestrel," *2018 AIAA Aerospace Sciences Meeting*, AIAA, 2018. doi:10.2514/6.2018-0534.

[52] McDaniel, D. R., and Morton, S. A., "Efficient Mesh Deformation for Computational Stability and Control Analysis on Unstructured Viscous Meshes," *47th AIAA Aerospace Sciences Meeting*, AIAA, 2009. doi:10.2514/6.2009-1363.

[53] Chourdakis, G., Davis, K., Rednberg, G., et al., "preCICE v2: A sustainable and user-friendly coupling library [version 2; peer review: 2 approved]," *Open Res Europe*, 2022, 2:51.

[54] Oliani, S., Casari, N., and M., C., "ICSFoam: An OpenFOAM library for implicit coupled simulations of high-speed flows." *Computer Physics Communications, Volume 286*, 2023, 108673.

[55] Chourdakis, G., Schneider, D., and Uekermann, B., "OpenFOAM-preCICE: Coupling OpenFOAM with External Solvers for Multi-Physics Simulations." *OpenFOAM® Journal 3, 1-25*, 2023.

[56] "soilds4Foam," URL=https://solids4foam.github.io, 2023.